2000PASJ...52..645H

PASJ: Publ. Astron. Soc. Japan **52**, 645–657 (2000)

Electrodynamic Structure of an Outer-Gap Accelerator: Invisibility of the TeV Emission from a Pulsar Magnetosphere

Kouichi HIROTANI

National Astronomical Observatory, Mitaka, Tokyo 181-8588
E-mail (FI): hirotani@hotaka.mtk.nao.ac.jp

(Received 1999 May 7; accepted 1999 August 23)

Abstract

We consider the γ-ray emissions from an outer-magnetospheric gap around a rotating neutron star. Migratory electrons and positrons are accelerated by the electric field exerted in the gap to radiate copious γ-rays via a curvature process. Some of these γ-rays materialize as pairs within the gap by colliding with the X-rays, leading to a pair-production cascade. The replenished charges partially screen the original acceleration field, which is self-consistently solved from the Poisson equation for the electrostatic potential. By considering the γ-ray spectrum explicitly, we compute the pair-production rate in the gap to solve the Boltzmann equations for γ-rays, together with the continuity equations for particles and the Poisson equation. It is demonstrate that the pulsed emission above 5 TeV due to the inverse Compton scatterings could not be detected by the current ground-based telescopes for ordinary pulsar parameters.

Key words: gamma-rays: theory — magnetic field — stars: neutron

1. Introduction

The EGRET experiment on the Compton Gamma Ray Observatory has detected pulsed signals from seven rotation-powered pulsars (for Crab Pulsar, Nolan et al. 1993; Fierro et al. 1998; for Vela Pulsar, Kanbach et al. 1994; Fierro et al. 1998; for Geminga, Mayer-Hasselwander et al. 1994; Fierro et al. 1998; for PSR B1706 − 44, Thompson et al. 1996; for PSR B1046 − 58; Kaspi at al. 2000; for PSR B1055 − 52, Thompson et al. 1999; for PSR B1951 + 32, Ramanamurthy et al. 1995; for reviews, e.g., Ulmer 1994; Nel et al. 1996; Nolan et al. 1996), with PSR B0656 + 14 being a possible detection (Ramanamurthy et al. 1996). The modulation of the γ-ray light curves at GeV energies testifies to the production of γ-ray radiation in the pulsar magnetospheres either at the polar cap (Harding et al. 1978; Daugherty, Harding 1982, 1996; Dermer, Sturner 1994; Sturner et al. 1995; Shibata et al. 1998; Miyazaki, Takahara 1997; also see Scharlemann et al. 1978 for the slot gap model), or at the vacuum gaps in the outer magnetosphere (Cheng et al. 1986a,b, hereafter CHR; Chiang, Romani 1992, 1994; Romani, Yadigaroglu 1995; Romani 1996; Zhang, Cheng 1998; Cheng, Zhang 1998). Effective γ-ray production in a pulsar magnetosphere may be extended to the very high energy (VHE) region above 100 GeV as well; however, the predictions of fluxes by the current models of γ-ray pulsars are not sufficiently conclusive (e.g., Cheng 1994). Whether or not the spectra of γ-ray pulsars continue up to the VHE region is a question which remains one of the interesting issues of high-energy astrophysics.

In the VHE region, positive detections of radiation at a high confidence level have been reported from the directions of the Crab, B1706 − 44, and Vela pulsars (Nel et al. 1993; Edwards et al. 1994; Yoshikoshi et al. 1997; see also Kifune 1996 for a review), by virtue of the technique of imaging Cerenkov light from extensive air showers. However, as for *pulsed* TeV radiation, only the upper limits have been, as a rule, obtained from these pulsars (see the references cited just above). If the VHE emission originates the pulsar magnetosphere, rather than the extended nebula, a significant fraction of them can be expected to show pulsation. Therefore, the lack of *pulsed* TeV emissions provides a severe constraint on the modeling of particle acceleration zones in a pulsar magnetosphere.

In fact, in CHR picture, the magnetosphere should be optically thick for pair-production in order to reduce the TeV flux to an unobserved level by absorption. This in turn requires very high luminosities of tertiary photons in the infrared energy range. However, the required fluxes are generally orders of magnitude larger than the observed values (Usov 1994). We are therefore motivated by the need to contrive an outer-gap model which produces less TeV emission with a moderate infrared luminosity.

High-energy emission from a pulsar magnetosphere, in fact, crucially depends on the acceleration electric field,

© Astronomical Society of Japan • Provided by the NASA Astrophysics Data System

2000PASJ...52..645H

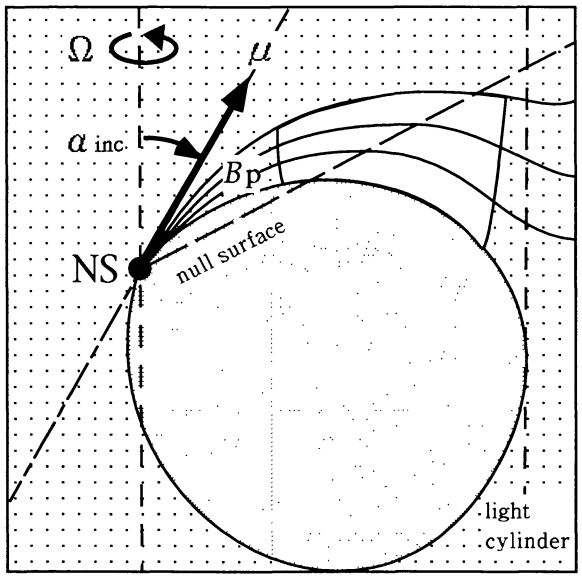

Fig. 1. Side view of a hypothetical outer-magnetospheric gap which is immersed in the surface blackbody X-ray radiation field. γ-ray photons are produced via a curvature radiation process.

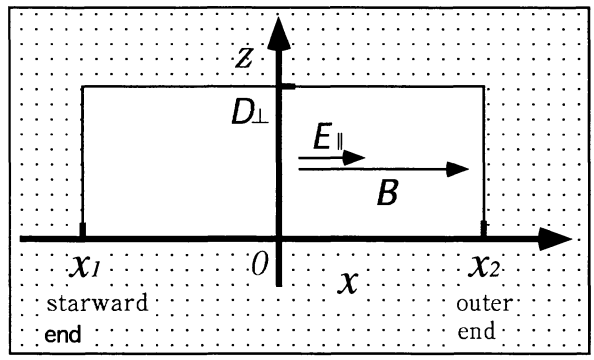

Fig. 2. Rectilinear approximation to the outer gap. The null surface is approximated by the z-axis ($x = 0$). The y-axis, which designates the azimuth, is not depicted to avoid complication.

$E_{\parallel}$, along the magnetic field lines. It was Hirotani and Shibata (1999a,b,c; hereafter Papers I, II, III) who first solved the spatial distribution of $E_{\parallel}$ together with particle and γ-ray distribution functions. They explicitly demonstrated that there is a stationary solution for an outer gap which is formed around the null surface at which the local Goldreich–Julian charge density,

$$\rho_{\rm GJ} = \frac{\Omega B_z}{2\pi c}, \tag{1}$$

vanishes, where B_z is the component of the magnetic field along the rotation axis, Ω refers to the angular frequency of the neutron star, and c is the speed of light. This expression of $\rho_{\rm GJ}$ holds if the electric field is approximated by the corotational field; this is, in turn, justified when the voltage drop in the gap is small compared with the available electromotive force exerted on a spinning neutron star surface, $V_* \sim 10^{15.5}{\Omega_2}^2\mu_{30}$ V. Equation (1) is valid unless the gap is located close to the light cylinder. Here, distance of the light cylinder from the rotation axis is given by

$$\varpi_{\rm LC} = 3 \times 10^8 {\Omega_2}^{-1} \text{ cm}, \tag{2}$$

where $\Omega_2 \equiv \Omega/(100 \text{ rad s}^{-1})$. See figure 1.

In this paper, we develop the method presented in Paper III in the sense that:
(1) We consider the effect of aberration when we compute the collision angles between the γ-rays and the X-rays (see subsubsection 2.4.1 for details),
(2) we take account of the projection effect of three-dimensional velocities on the poloidal plan when we write down the Boltzmann equations for particles (subsection 2.5) and for γ-rays (subsection 2.6),
(3) we consider hard blackbody and power-law X-ray components in addition to the soft blackbody one (subsubsection 2.4.3 and 2.4.4).

In the next section, we discuss the physical processes of pair production cascade in the outer magnetosphere of a pulsar and present basic equations describing the system. We then solve these equations in section 3 and reveal that the flux of TeV γ-rays produced via inverse-Compton scatterings will be well below the observational upper limit. In the final section, we discuss the validity of the assumptions.

2. Basic Equations and Boundary Conditions

To investigate the gap structure quantitatively, we first reduce the Poisson equation for the electric potential into a one-dimensional form in subsection 2.1. We then give a curvature-limited Lorentz factor in subsection 2.2. The X-ray field illuminating the gap is described in subsection 2.3, which is important to deduce the pair-production mean-free path in subsection 2.4. We solve the Boltzmann equations of electrons/positrons in subsection 2.5 and those of γ-ray photons in subsection 2.6, and impose suitable boundary conditions in subsection 2.7.

2.1. *Reduction of the Poisson Equation*

To simplify the geometry, let us introduce a rectilinear approximation for a region around the null surface. Suppose that the magnetic field lines are straight lines parallel to the x-axis (figure 2). Here, x is an outward

© Astronomical Society of Japan • Provided by the NASA Astrophysics Data System

2000PASJ...52..645H

increasing coordinate along a magnetic field line, while y designates the azimuth. We approximate the null surface by the z-axis ($x = 0$). By using this rectilinear coordinates, the Poisson equation for the non-corotating electric potential Φ becomes

$$-\left(\frac{\partial^2}{\partial x^2}+\frac{\partial^2}{\partial y^2}+\frac{\partial^2}{\partial z^2}\right)\Phi(x,y,z) = 4\pi[e(N_+ - N_-) - \rho_{\rm GJ}], \tag{3}$$

where N_+ and N_- are the spatial number densities of e^+'s and e^-'s, respectively; e refers to the magnitude of the charge on the electron. If the trans-field thickness of the gap D_z is sufficiently large compared to the longitudinal thickness of the gap, we can neglect the z-dependence of quantities, that is, $\partial^2/\partial z^2 = 0$. However, D_z, which is determined by quantum electrodynamic processes, can be as large as the longitudinal thickness. To consider these effects, we use an approximation, $\partial^2\Phi/\partial z^2 = -\Phi/{D_z}^2$ (Michel 1974). This approximation stands for the fact that the accelerating region is bounded at $z = 0$ and $z = D_z$ by the conducting side walls that are grounded to the star on which Φ vanishes.

In the same manner, we Fourier analyze all the quantities in the azimuthal direction and replace $\partial^2/\partial y^2$ with $-m^2$, where m is an integer from the periodic boundary condition. On these grounds, we replace ${\partial_y}^2 + {\partial_z}^2$ with $-{D_\perp}^{-2} \equiv -m^2 - {D_z}^{-2}$ and focus attention on the gap structure in the x direction (i.e., along the magnetic field lines).

The primary effect of field line curvature appears in the x-dependence of $\rho_{\rm GJ}$. Thus, we arrive at the following Poisson equation in the first order approximation:

$$-\frac{d^2\Phi}{dx^2} = -\frac{\Phi}{D_\perp^2} + 4\pi[e(N_+ - N_-) - \rho_{\rm GJ}]. \tag{4}$$

It is convenient to non-dimensionalize the length scales by a typical Debye scale length $c/\omega_{\rm p}$ (see the discussion in subsection 3.1 in Paper I for details), where

$$\omega_{\rm p} = \sqrt{\frac{4\pi e^2}{m_{\rm e}}\frac{\Omega B}{2\pi c e}} = 1.875\times 10^7 {\Omega_2}^{1/2}{B_5}^{1/2}\ {\rm rad\ s^{-1}}, \tag{5}$$

where B_5 is the magnetic field at the null surface normalized by 10^5 G.

Let us introduce the following dimensionless coordinate variable:

$$\xi \equiv \frac{\omega_{\rm p}}{c}x = 6.25\times 10^{-4}{\Omega_2}^{1/2}{B_5}^{1/2}x, \tag{6}$$

where x is measured in cm. We are considering a gap which is not very close to the light cylinder. We thus approximate B_5 with the Newtonian dipole field to obtain

$$B_5 = 0.37\sqrt{1+3\cos^2(\theta_0-\alpha_{\rm i})}\left(\frac{r_0}{\varpi_{\rm LC}}\right)^{-3}\mu_{30}{\Omega_2}^3, \tag{7}$$

where μ_{30} refers to the magnetic moment μ in the unit of 10^{30} G cm^3, and $\alpha_{\rm i}$ to the inclination angle; (r_0, θ_0) indicates the polar coordinates of the intersection of the null surface and the last open field line in the poloidal plane. They are defined by

$$\frac{r_0}{\varpi_{\rm LC}} \equiv \frac{4}{4+\tan^2\theta_0} \times \frac{2\tan^2\alpha_{\rm i}+3+\sqrt{9+8\tan^2\alpha_{\rm i}}}{(4/3)\tan^2\alpha_{\rm i}+3+\sqrt{9+8\tan^2\alpha_{\rm i}}}, \tag{8}$$

$$\tan\theta_0 \equiv \frac{3\tan\alpha_{\rm i}+\sqrt{9\tan^2\alpha_{\rm i}+8}}{2}. \tag{9}$$

To fix the proportionality coefficient, $\xi/x \propto \sqrt{\Omega_2 B_5}$, we evaluate it at the null surface. Its value there depends on the three magnetospheric parameters: Ω, μ, and $\alpha_{\rm i}$. For example, when $\Omega = 10^2$ rad s^{-1} and $\mu = 10^{30}$ G cm^3, we obtain $\xi = 8.31\times 10^{-4}x$ if $\alpha_{\rm i} = 0°$, while $\xi = 1.97\times 10^{-3}x$ if $\alpha_{\rm i} = 30°$, and $\xi = 4.91\times 10^{-4}x$ if $\alpha_{\rm i} = -30°$.

By using ξ, we can simplify the Poisson equation (4) to the form

$$E_\parallel = -\frac{d\varphi}{d\xi} \tag{10}$$

and

$$\frac{dE_\parallel}{d\xi} = -\frac{\varphi}{{\Delta_\perp}^2} + n_+(\xi) - n_-(\xi) - \frac{2\pi c}{\Omega B}\rho_{\rm GJ}(\xi), \tag{11}$$

where

$$\Delta_\perp \equiv \frac{\omega_{\rm p}}{c}D_\perp; \tag{12}$$

the dimensionless electrostatic potential and electric field are defined by

$$\varphi(\xi) \equiv \frac{e\Phi(x)}{m_{\rm e}c^2}, \tag{13}$$

$$E_\parallel \equiv -\frac{d\varphi}{d\xi} = -\frac{e}{m_{\rm e}c\omega_{\rm p}}\frac{d\Phi}{dx} = 3.12\times 10^{-5}\left(\frac{d\Phi/dx}{\rm V\ m^{-1}}\right)\frac{1}{\sqrt{\Omega_2 B_5}}, \tag{14}$$

and the particle densities are normalized in terms of a typical value of the Goldreich–Julian density defined by B (instead of B_z) as follows:

$$n_\pm(\xi) \equiv \frac{2\pi c e}{\Omega B}N_\pm(x). \tag{15}$$

For a Newtonian dipole field, the Goldreich–Julian charge density becomes

$$\frac{2\pi c}{\Omega B}\rho_{\rm GJ} = \frac{2\cos\theta\cos(\theta-\alpha_{\rm inc}) - \sin\theta\sin(\theta-\alpha_{\rm inc})}{\sqrt{1+3\cos^2\theta}\,[1-(\Omega\varpi/c)^2]}, \tag{16}$$

where θ refers to the polar angle of the position at which $\rho_{\rm GJ}$ is measured, and ϖ indicates the distance of the

© Astronomical Society of Japan • Provided by the NASA Astrophysics Data System

2000PASJ...52..645H

point from the rotation axis. As we shall see, the gap half width along the field lines is typically less than 15% of $\varpi_{\rm LC}$, we can evaluate θ under the rectilinear approximation as

$$\theta = \sin^{-1}\left(\frac{r_0 \sin\theta_0 + x}{r}\right), \tag{17}$$

where r denotes the distance of the position from the star, and is given by

$$r = \sqrt{{r_0}^2 \cos^2\theta_0 + (r_0 \sin\theta_0 + x)^2}. \tag{18}$$

We also have $\varpi = r \sin\theta = r_0 \sin\theta_0 + x$.

2.2. Terminal Lorentz Factor

The most effective assumption for particle motion in the gap arises from the fact that the velocity immediately saturates in the balance between the electric force and the radiation reaction force due to curvature radiation. Equating the electric force, $e|d\Phi/dx|$, and the radiation reaction force with the radius of curvature, $R_{\rm c}$, we obtain the saturated Lorentz factor at each point, as follows:

$$\Gamma = \left(\frac{3{R_{\rm c}}^2}{2e}\left|\frac{d\Phi}{dx}\right| + 10^{24}\right)^{1/4}, \tag{19}$$

where the second term 10^{24} is added for a realistic treatment of the boundaries of the gap. Near the boundaries, where the diminished electric field no longer contributes to the force balance, radiation reaction damps the Lorentz factor. Since the damping length is larger than the width of the boundary regions, Γ is kept over 10^6 in these regions. (Without the 10^{24} term, the vanishing electric field would lead to the vanishment of Γ at the boundaries.)

2.3. X-Ray Field

Before proceeding to a discussion on the pair-production mean-free path, it is desirable to describe the X-ray field that illuminates the outer gap. The X-ray field of a rotation-powered neutron star within the light cylinder can be attributed to the following three emission processes:

(1) Photospheric emission from the whole surface of a cooling neutron star (Greenstein, Hartke 1983; Romani 1987; Shibanov et al. 1995; Pavlov et al. 1994; Zavlin et al. 1995a).

(2) Thermal emission from the neutron star's polar caps, which are heated by the bombardment of relativistic particles streaming back to the surface from the magnetosphere (Kundt, Schaaf 1993; Zavlin et al. 1995b; Gil, Krawczyk 1996).

(3) Non-thermal emission from relativistic particles accelerated in the pulsar magnetosphere (Ochelkov, Usov 1980a,b; El-Gowhari, Arponen 1972; Aschenbach, Brinkmann 1974; Hardee, Rose 1974; Daishido 1975).

The spectrum of the first component is expected to be expressed by a modified blackbody. However, for simplicity, we approximate it in terms of a Planck function with temperature $kT_{\rm s}$, because the X-ray spectrum is occasionally fitted by a simple blackbody spectrum. We regard a blackbody component as the first one if its observed emitting area is comparable with the whole surface of a neutron star, $A_* \equiv 4\pi {r_*}^2$, where r_* denotes the neutron star radius. We take account of both the pulsed and the unpulsed surface blackbody emission as this soft blackbody component.

As for the second component, we regard a blackbody component as the heated polar cap emission if its observed emitting area is much smaller than A_*. We approximate its spectrum by a Planck function. We take account of both the pulsed and the unpulsed polar cap emission as this hard blackbody component.

Unlike the first and the second components, a power-law component is usually dominated by nebula emission. To get rid of the nebula emission, which illuminates the outer gap inefficiently, we adopt only the pulsed components of a power-law emission as the third component.

2.4. Pair-Production Mean-Free Path

In this subsection, we draw attention to how the pair-production mean-free path is related with the X-ray field described in the previous section. To this end, we first give the threshold energy for X-ray photons to materialize. Then, we consider the mean-free path for a γ-ray photon to materialize as a pair in a collision with one of the soft blackbody X-rays in subsubsection 2.4.2, the hard blackbody ones in subsubsection 2.4.3, and the magnetospheric, power-law X-rays in subsubsection 2.4.4. We finally summarize how the real mean-free path should be computed under the existence of these three X-ray components in subsubsection 2.4.5.

2.4.1. Threshold energy

The threshold energy for a soft photon to materialize as a pair in a collision with a γ-ray photon having energy $m_{\rm e}c^2\epsilon_\gamma = E_{\rm c}$, is given by

$$E_{\rm th} = \frac{2}{1-\mu_{\rm c}}\frac{m_{\rm e}c^2}{\epsilon_\gamma}, \tag{20}$$

where $\mu_{\rm c}$ refers to the cosine of the three-dimensional collisional angle between the X-rays and the γ-rays. The lower bound of $2/(1-\mu_{\rm c})$ is unity, which is realized if the two photons head-on collide.

To evaluate $\mu_{\rm c}$, we must consider a γ-ray's toroidal momenta due to an aberration. It should be noted that a γ-ray photon propagates in the instantaneous direction of the particle motion at the time of the emission. The

© Astronomical Society of Japan • Provided by the NASA Astrophysics Data System

2000PASJ...52..645H

toroidal velocity of a particle at the gap center (r_0, θ_0) becomes

$$v_\phi = r_0 \sin\theta_0 \Omega + \kappa B_\phi - E_\parallel \times B_\phi \frac{c}{B^2}, \tag{21}$$

where κ is a constant. On the right-hand side, the first term is due to corotation, while second one due to magnetic bending. Since $E_\parallel$ arises in the gap, the corresponding drift velocity appears as the third term. Unless the gap is located close to the light cylinder, we can neglect the terms containing B_ϕ as a first-order approximation. We thus have $v_\phi = r_0 \sin\theta_0 \Omega$. Since the three-dimensional particle velocity is virtually c, the angle between the particle motion and the poloidal plane becomes

$$\phi_{\rm ab} = \sin^{-1}\left(\frac{r_0 \sin\theta_0 \Omega}{c}\right) = \sin^{-1}\left(\frac{r_0 \sin\theta_0}{\varpi_{\rm LC}}\right). \tag{22}$$

In the case of $\alpha_{\rm i} = 30°$, we obtain $\phi_{\rm ab} = 21.°8$. When $\alpha_{\rm i} = 30°$, the collisional angle on the poloidal plane becomes $\theta_{\rm c} = 90° - \theta_0 = 21.°6$ when outwardly propagating γ-rays collide with the X-rays emitted from the neutron star surface; θ_0 can be computed by equation (9). Therefore, we obtain $\mu_{\rm c} = \cos\phi_{\rm ab} \sin\theta_{\rm c} = 0.342$. It should be noted that the collision angle between *inward* propagating γ-rays and the X-rays emitted from the neutron star surface becomes $-\mu_{\rm c}$.

2.4.2. *Soft blackbody component*

We first consider the pair-production mean-free path, $\lambda_{\rm s}$, for a γ-ray photon to materialize in a collision with one of the *soft* blackbody X-rays. For outwardly propagating γ-rays, $\lambda_{\rm s}$ is given by (Hirotani 2000a, b; hereafter Papers IV, V):

$$\frac{1}{\lambda_{\rm s}^+} = \int_{2/(1-\mu_{\rm c})\epsilon_\gamma}^\infty d\epsilon_{\rm x} \frac{dN_{\rm s}}{d\epsilon_{\rm x}} \sigma_{\rm p}(\epsilon_\gamma, \epsilon_{\rm x}, \mu_{\rm c}), \tag{23}$$

whereas for inwardly propagating γ-rays,

$$\frac{1}{\lambda_{\rm s}^-} = \int_{2/(1+\mu_{\rm c})\epsilon_\gamma}^\infty d\epsilon_{\rm x} \frac{dN_{\rm s}}{d\epsilon_{\rm x}} \sigma_{\rm p}(\epsilon_\gamma, \epsilon_{\rm x}, \mu_{\rm c}), \tag{24}$$

where $\mu_{\rm c} = 0.345$ for $\alpha_{\rm i} = 30°$; the pair-production cross section is given by (Berestetskii et al. 1989)

$$\sigma_{\rm p}(\epsilon_\gamma, \epsilon_{\rm x}, \mu_{\rm c}) \equiv \frac{3}{16}\sigma_{\rm T}(1-v^2)\left[(3-v^4)\ln\frac{1+v}{1-v} - 2v(2-v^2)\right], \tag{25}$$

$$v(\epsilon_\gamma, \epsilon_{\rm x}, \mu_{\rm c}) \equiv \sqrt{1 - \frac{2}{1-\mu_{\rm c}}\frac{1}{\epsilon_\gamma \epsilon_{\rm x}}}. \tag{26}$$

Here, $\sigma_{\rm T}$ is the Thomson cross section, and $\epsilon_{\rm x} \equiv E_{\rm x}/m_{\rm e}c^2$ refers to the non-dimensional energy of an X-ray photon. We may notice here that the non-dimensional threshold energy $E_{\rm th}/(m_{\rm e}c^2)$ appears in the lower bound of the integral in equations (23) and (24).

The number density of soft X-rays between energy $m_{\rm e}c^2\epsilon_{\rm x}$ and $m_{\rm e}c^2(\epsilon_{\rm x} + d\epsilon_{\rm x})$ at a position x is given by the Planck law,

$$\frac{dN_{\rm s}}{d\epsilon_{\rm x}} = \left[1 + 2\frac{x}{\varpi_{\rm LC}}\sin\theta_0 + \left(\frac{x}{\varpi_{\rm LC}}\right)^2\right]\left(\frac{dN_{\rm s}}{d\epsilon_{\rm x}}\right)_0, \tag{27}$$

where

$$\left(\frac{dN_{\rm s}}{d\epsilon_{\rm x}}\right)_0 = \frac{1}{4\pi^2}\left(\frac{m_{\rm e}c^2}{c\hbar}\right)^3\left(\frac{A_{\rm s}}{4\pi r_0^2}\right) \times \frac{{\epsilon_{\rm x}}^2}{\exp(\epsilon_{\rm x}/\Delta_{\rm s}) - 1}, \tag{28}$$

is evaluated at the gap center ($x = 0$); $A_{\rm s}$ indicates the observed radius of the blackbody-emitting region and $\Delta_{\rm s}$ is defined by

$$\Delta_{\rm s} \equiv \frac{kT_{\rm s}}{m_{\rm e}c^2}, \tag{29}$$

where $kT_{\rm s}$ refers to the soft blackbody temperature measured by a distant observer. Since the outer gap is located outside of the deep gravitational potential well of the neutron star, the photon energy there is essentially the same as that which a distant observer measures.

2.4.3. *Hard blackbody component*

In this subsection, let us consider the case when the X-ray field is dominated by the *hard* blackbody component. In the same manner as the soft blackbody component, the *hard* blackbody component gives the following mean-free path for pair production:

$$\frac{1}{\lambda_{\rm h}^\pm} \equiv \int_{2/(1\mp\mu_{\rm c})\epsilon_\gamma}^\infty d\epsilon_{\rm x} \frac{dN_{\rm h}}{d\epsilon_{\rm x}} \sigma_{\rm p}(\epsilon_\gamma, \epsilon_{\rm x}, \mu_{\rm c}), \tag{30}$$

where $\mu_{\rm c}$ takes the same value as in the soft-blackbody-dominated case. The upper and lower signs correspond to the outwardly and inwardly propagating γ-rays, respectively. The number density of the hard X-rays between energy $m_{\rm e}c^2\epsilon_{\rm x}$ and $m_{\rm e}c^2(\epsilon_{\rm x} + d\epsilon_{\rm x})$ at a position x is given by the Planck law,

$$\frac{dN_{\rm h}}{d\epsilon_{\rm x}} = \left[1 + 2\frac{x}{\varpi_{\rm LC}}\sin\theta_0 + \left(\frac{x}{\varpi_{\rm LC}}\right)^2\right]\left(\frac{dN_{\rm h}}{d\epsilon_{\rm x}}\right)_0, \tag{31}$$

where

$$\left(\frac{dN_{\rm h}}{d\epsilon_{\rm x}}\right)_0 = \frac{1}{4\pi^2}\left(\frac{m_{\rm e}c^2}{c\hbar}\right)^3\left(\frac{A_{\rm h}}{4\pi r_0^2}\right) \times \frac{{\epsilon_{\rm x}}^2}{\exp(\epsilon_{\rm x}/\Delta_{\rm h}) - 1}; \tag{32}$$

where $A_{\rm h}$ is the observed emission area of the hard-blackbody emission. $\Delta_{\rm h}$ is defined by

$$\Delta_{\rm h} \equiv \frac{kT_{\rm h}}{m_{\rm e}c^2}, \tag{33}$$

where $kT_{\rm h}$ refers to the hard blackbody temperature measured by a distant observer.

© Astronomical Society of Japan • Provided by the NASA Astrophysics Data System

2000PASJ...52..645H

2.4.4. Power-law component

The secondary X-ray photons emitted outside of the gap via synchrotron process will be beamed in the propagation direction of the primary γ-rays. Thus, the collision angle between a secondary X-ray photon and a primary γ-ray photon can be evaluated by the angle between the propagation direction of the γ-rays (γ_1, say) that has materialized to emit the secondary X-rays and the another γ-rays (γ_2, say). The collision angle will therefore be the directional difference of the magnetic field at the places where γ_1 and γ_2 are emitted. Evaluating the distance between the two places as the gap half width, the typical collision angle can be approximated as $h \equiv H/\varpi_{\rm LC}$ rad. As shown in section 3, the dimensionless gap half width, h, becomes typically around 0.1. We thus assume in this paper that the collision angle between the γ-rays and the magnetospheric, power-law X-rays is 0.1 rad. It follows that the mean-free path for a γ-ray photon to materialize in a collision with one of the magnetospheric X-rays becomes

$$\frac{1}{\lambda_{\rm pl}} = \int_{\zeta/\epsilon_\gamma}^{\infty} d\epsilon_{\rm x} \frac{dN_{\rm pl}}{d\epsilon_{\rm x}} \sigma_{\rm p}(\epsilon_\gamma, \epsilon_{\rm x}, \mu_{\rm c}), \tag{34}$$

where

$$\zeta \equiv \frac{2}{1-\mu_{\rm c,pl}} \tag{35}$$

with $\mu_{\rm c,pl} = \cos(0.1)$. We represent the power-law spectrum as

$$\frac{dN_{\rm pl}}{d\epsilon_{\rm x}} = N_{\rm pl}{\epsilon_{\rm x}}^{\alpha} \quad (\epsilon_{\rm min} < \epsilon_{\rm x} < \epsilon_{\rm max}). \tag{36}$$

The photon index, α, is typically between -2 and -1 for a pulsed, power-law X-ray component in hard X-ray band (e.g., Saito 1998).

2.4.5. Pair-production mean-free path

The true mean-free path, $\lambda_{\rm p}$, is determined by the component that dominates the X-ray field, or equivalently, the smallest one among $\lambda_{\rm s}$, $\lambda_{\rm h}$, and $\lambda_{\rm pl}$. Therefore, we can evaluate $\lambda_{\rm p}$ as

$$\frac{1}{\lambda_{\rm p}} = \frac{1}{\lambda_{\rm s}} + \frac{1}{\lambda_{\rm h}} + \frac{1}{\lambda_{\rm pl}}. \tag{37}$$

When a pulsar is young, the third term will dominate because of its strong magnetospheric emission. As the pulsar evolves, the first term becomes dominant because of the rapid decrease of the magnetospheric emission due to spindown. However, as the pulsar evolves further, polar cap heating due to particle bombardment begins to dominate; therefore, the second term will be important at last.

2.5. Boltzmann Equations for Particles

The number density of positrons (N_+) or electrons (N_-) follows one-dimensional continuity equation with a source term; the particles are supplied by the photon–photon pair-production process. It should be noted that almost all the particles migrate with the large, saturated Lorentz factor. We therefore assume for simplicity that both electrostatic and curvature-radiation-reaction forces cancel out each other and obtain the following continuity equations in the rectilinear coordinates:

$$+c(1-q)\frac{dN_+}{dx} = \int_0^\infty d\epsilon_\gamma \left[\eta_{\rm p+} G_+(x,\epsilon_\gamma) + \eta_{\rm p-} G_-(x,\epsilon_\gamma)\right], \tag{38}$$

$$-c(1-q)\frac{dN_-}{dx} = \int_0^\infty d\epsilon_\gamma \left[\eta_{\rm p+} G_+(x,\epsilon_\gamma) + \eta_{\rm p-} G_-(x,\epsilon_\gamma)\right], \tag{39}$$

$$q \equiv \frac{1}{2}\left(\frac{\varpi}{\varpi_{\rm LC}}\right)^2, \tag{40}$$

where $N_\pm(x)$ are the spatial number density of $e^\pm$'s, and $G_\pm$ are the distribution function of γ-ray photons having momentum $\pm m_{\rm e} c \epsilon_\gamma$ along the poloidal field line; the factor $1-q$ denotes the projection effect due to the three-dimensional motion of the particles. In general, $\cos\phi_{\rm ab}$ appears instead of $(1-q)$ in the left-hand side. Expanding it around $\phi_{\rm ab} = 0$, we obtain (40) with the aid of (22). Since the electric field is assumed to be positive in the gap, e^+'s (or e^-'s) migrate outwards (or inwards). The particles are assumed to lose their initial momenta shortly after their birth; that is, a positron and an electron are supposed to split into opposite directions at the place of pair production. $\eta_{\rm p+}$ (or $\eta_{\rm p-}$) refers to the pair-production redistribution function for outward (or inward) propagating γ-rays. The dimensionless pair-production rate, $\eta_{\rm p\pm}$, is related with the mean-free path as follows:

$$\eta_{\rm p\pm}(\epsilon_\gamma, \xi) = \frac{c}{\omega_{\rm p}} \frac{1}{\lambda_{\rm p}^{\pm}(\xi)}. \tag{41}$$

Let us introduce the following dimensionless γ-ray densities in the dimensionless energy interval between β_{i-1} and β_i such that

$$g_\pm{}^i(\xi) \equiv \frac{2\pi c e}{\Omega B} \int_{\beta_{i-1}}^{\beta_i} d\epsilon_\gamma G_\pm(x,\epsilon_\gamma), \tag{42}$$

where $\Omega B/(2\pi c e)$ is a typical value of the Goldreich–Julian number density of particles. In this paper, we set $\beta_0 = 1$, which corresponds to the lowest γ-ray energy, 0.511 MeV. To cover a wide range of γ-ray energies, we divide the γ-ray spectra into 14 energy bins

© Astronomical Society of Japan • Provided by the NASA Astrophysics Data System

2000PASJ...52..645H

and put $\beta_1 = 1.0 \times 10^1$, $\beta_2 = 3.0 \times 10^1$, $\beta_3 = 1.0 \times 10^2$, $\beta_4 = 2.0 \times 10^2$, $\beta_5 = 3.0 \times 10^2$, $\beta_6 = 6.0 \times 10^2$, $\beta_7 = 1.0 \times 10^3$, $\beta_8 = 2.0 \times 10^3$, $\beta_9 = 3.0 \times 10^3$, $\beta_{10} = 6.0 \times 10^3$, $\beta_{11} = 1.0 \times 10^4$, $\beta_{12} = 2.0 \times 10^4$, $\beta_{13} = 3.0 \times 10^4$, $\beta_{14} = 1.0 \times 10^5$. Provided that the blackbody temperature is roughly 100 eV, only γ-rays having energies

$$m_e c^2 \epsilon_\gamma > 10^3 \left(\frac{kT}{100\ \mathrm{eV}}\right)^{-1} m_e c^2 \approx 0.5 \left(\frac{kT}{100\ \mathrm{eV}}\right)^{-1} \mathrm{GeV} \tag{43}$$

can contribute for pair production.

We can rewrite equations (38) and (39) into the dimensionless forms:

$$(1-q)\frac{dn_+}{d\xi} = +\sum_{i=1}^{14}[\eta_{\mathrm{p}+}^i g_+^i(\xi) + \eta_{\mathrm{p}-}^i g_-^i(\xi)], \tag{44}$$

$$(1-q)\frac{dn_-}{d\xi} = -\sum_{i=1}^{14}[\eta_{\mathrm{p}+}^i g_+^i(\xi) + \eta_{\mathrm{p}-}^i g_-^i(\xi)], \tag{45}$$

where $\eta_{\mathrm{p}\pm}^i$ are evaluated at the central energy in each bin and are defined as

$$\eta_{\mathrm{p}\pm}^i \equiv \frac{1}{\omega_{\mathrm{p}}}\eta_{\mathrm{p}\pm}\left(\frac{\beta_{i-1}+\beta_i}{2}\right); \tag{46}$$

$n_\pm(\xi) \equiv (2\pi ce/\Omega B)N_\pm(x)$ is normalized with the same factor as $g_\pm^i(\xi)$.

A combination of equations (44) and (45) gives the current conservation law,

$$j_0 \equiv n_+(\xi) + n_-(\xi) = \text{constant for } \xi. \tag{47}$$

When $j_0 = 1.0$, the current density equals the typical Goldreich–Julian current density, $\Omega B/(2\pi)$.

2.6. Boltzmann Equations for Gamma-Rays

Let us next discuss the Boltzmann equations which the γ-ray distribution functions obey. In the rectilinear approximation, γ-ray photons are considered to be directed only in the $\pm x$-direction due to relativistic beaming. We thus approximate the γ-ray Boltzmann equations into the one-dimensional form

$$\pm c(1-q)\frac{\partial}{\partial x}G_\pm(x,\epsilon_\gamma) = -\eta_{\mathrm{p}\pm}G_\pm(x,\epsilon_\gamma) + \eta_{\mathrm{c}}N_\pm(x), \tag{48}$$

where (e.g., Rybicki, Lightman 1979)

$$\eta_{\mathrm{c}} \equiv \frac{\sqrt{3}e^2\Gamma}{hR_{\mathrm{c}}}\frac{1}{\epsilon_\gamma}F\left(\frac{\epsilon_\gamma}{\epsilon_{\mathrm{c}}}\right), \tag{49}$$

$$\epsilon_{\mathrm{c}} \equiv \frac{1}{m_e c^2}\frac{3}{4\pi}\frac{hc\Gamma^3}{R_{\mathrm{c}}}, \tag{50}$$

$$F(s) \equiv s\int_x^\infty K_{\frac{5}{3}}(t)dt, \tag{51}$$

where R_{c} is the curvature radius of the magnetic field lines. The effect of the broad spectrum of curvature γ-rays is represented by the factor $F(\epsilon_\gamma/\epsilon_{\mathrm{c}})$ in equation (49).

Integrating (48) in the energy intervals $[\beta_{i-1}, \beta_i]$, we obtain

$$\pm(1-q)\frac{d}{d\xi}g_\pm^i(\xi) = -\eta_{\mathrm{p}\pm}^i g_\pm^i(\xi) + \eta_{\mathrm{c}}^i n_\pm(\xi), \tag{52}$$

where $i = 1, 2, \cdots, m$ and

$$\eta_{\mathrm{c}}^i \equiv \frac{\sqrt{3}e^2\Gamma}{\omega_{\mathrm{p}}hR_{\mathrm{c}}}\int_{\beta_{i-1}/\epsilon_{\mathrm{c}}}^{\beta_i/\epsilon_{\mathrm{c}}} ds \int_s^\infty K_{\frac{5}{3}}(t)dt = 2.14\times10^{-8}\,\Gamma\left(\frac{R_{\mathrm{c}}}{0.5\varpi_{\mathrm{LC}}}\right)^{-1}\sqrt{\frac{\Omega_2}{B_5}} \times \int_{\beta_{i-1}/\epsilon_{\mathrm{c}}}^{\beta_i/\epsilon_{\mathrm{c}}} ds \int_s^\infty K_{\frac{5}{3}}(t)dt. \tag{53}$$

We may notice here that the ratio

$$\frac{\eta_{\mathrm{c}}^i}{\eta_{\mathrm{p}\pm}{}^i} \approx \frac{10^{-8}\Gamma\Omega_2^{1/2}B_5^{-1/2}}{10^4\delta^2\Omega_2^{3/2}B_5^{-1/2}} \approx 10^3\left(\frac{\Gamma}{10^7}\right)\left(\frac{kT}{100\ \mathrm{eV}}\right)^{-2}\Omega_2{}^{-1} \tag{54}$$

is much greater than unity unless Γ is sufficiently less than 10^7. Therefore, the γ-ray production term dominates the γ–γ absorption terms of equation (52).

The migrating $e^\pm$'s and the γ-ray photons in the gap are described by $2m+4$ differential equations (10), (11), (44), (45), and (52). It is worth noting that n^+ and n^- are related through the current conservation relation (47). To solve these equations, we shall impose some boundary conditions in the next subsection.

2.7. Boundary Conditions

Let us first consider the conditions at the *inner* (starward) boundary $\xi = \xi_1$. For one thing, the inner boundary is defined as the place where $E_\parallel$ vanishes. Therefore, we have

$$E_\parallel(\xi_1) = 0. \tag{55}$$

It is noteworthy that condition (55) is consistent with the stability condition at the plasma–vacuum interface if the electrically supported magnetospheric plasma is completely-charge-separated, i.e., if the plasma cloud at $x < x_1$ is composed of electrons alone (Krause-Polstorff, Michel 1985a,b).

Further, we put the value of Φ to be zero at the inner boundary,

$$\varphi(\xi_1) = 0. \tag{56}$$

© Astronomical Society of Japan • Provided by the NASA Astrophysics Data System

2000PASJ...52..645H

What is more, we impose for simplicity that no γ-rays capable of pair production enter from the outside of the gap; that is,

$$g_+^i(\xi_1) = 0 \quad (i = 1, 2, \cdots, m). \tag{57}$$

One final point is that we can impose conditions on n_+ and n_-. Assuming the negatively charged cloud at $x < x_1$ is composed of pure electrons, we can expect no influx of positrons, which are migrating $+x$ direction in the gap, at the inner boundary. Therefore, we obtain

$$n_+(\xi_1) = 0, \tag{58}$$

which yields with the help of the charge-conservation law (47),

$$n_-(\xi_1) = j_0. \tag{59}$$

We next consider the conditions at the *outer* boundary. The outer boundary, $\xi = \xi_2$, is defined so that $E_\parallel$ vanishes again. That is,

$$E_\parallel(\xi_2) = 0. \tag{60}$$

In the same manner at $\xi = \xi_1$, we impose both

$$g_-^i(\xi_2) = 0 \quad (i = 1, 2, \cdots, m) \tag{61}$$

and

$$n_-(\xi_2) = 0. \tag{62}$$

We have totally $2m + 6$ boundary conditions (55)–(62) for $2m + 4$ unknown functions Φ, $E_\parallel$, n_+, n_-, ${g_+}^1$, ${g_+}^2$, $\cdots$, ${g_+}^m$, ${g_-}^1$, ${g_-}^2$, $\cdots$, ${g_-}^m$. Thus two extra boundary conditions must be compensated by making the positions of the boundaries ξ_1 and ξ_2 be free. The two free boundaries appear because $E_\parallel = 0$ is imposed at the *both* boundaries and because j_0 is externally imposed.

In short, for a fixed X-ray field, the gap structure is described in terms of the following five dimensionless parameters:

$$j_0 \equiv n_+ + n_-, \tag{63}$$

$$\eta_{\mathrm{p}\pm}^i \propto {\Omega_2}^{3/2} {B_5}^{-1/2} \tag{64}$$

$$\eta_{\mathrm{c}}^i \propto \frac{R_{\mathrm{c}}}{c/\omega_{\mathrm{p}}}, \tag{65}$$

$$\Delta_\perp \equiv D_\perp/(c/\omega_{\mathrm{p}}) \propto D_\perp(\Omega B)^{-1/2}, \tag{66}$$

$$\alpha_{\mathrm{i}}. \tag{67}$$

The X-ray field affects the gap structure through $\eta_{\mathrm{p}\pm}^i$ ($i = 1, 2, \cdots, m$). It is noteworthy that j_0 is a free parameter in this paper, because it can be determined only from a global condition of the current circuit (e.g., Shibata 1997).

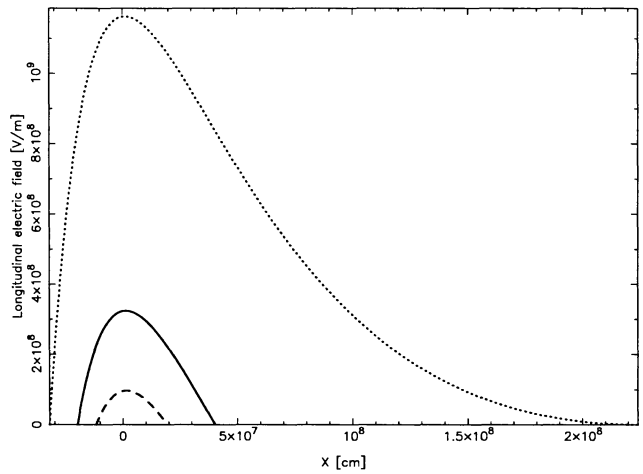

Fig. 3. The distribution of the acceleration field along the field line. For the solid line, $kT_{\mathrm{s}} = 50$ eV, while for the dashed and the dotted one, 100 and 23.5 eV, respectively. The hard blackbody and the power-law components are not included in this calculation.

3. Results

3.1. Electric Field Structure

We first consider the acceleration field $E_\parallel$ as a function of the position x for several values of the soft blackbody temperature, kT_{s}. In figure 3, we present the results of $E_\parallel(x)$ for $kT_{\mathrm{s}} = 70$ eV (solid curve), 100 eV (dashed one), and 23.5 eV (dotted one); the abscissa is in centimeter. In this calculation, neither the hard blackbody component nor the power-law component is not included. The parameters are fixed for these three curves as $\Omega = 100$ rad s^{-1}, $\mu = 10^{30}$ G cm^3.

It follows from this figure that the acceleration field increases as kT_{s} deceases; this result is consistent with previous works (Papers I, II, III, IV, and V). Moreover, the gap extends mainly in the positive x region for a small kT_{s}, because the X-ray field is diluted as the distance from the star increases. Below a certain value of kT_{s} ($= 23.5$ eV in the case of the present parameter set, as indicated by the dotted line), there is no solution that satisfies the boundary conditions described in subsection 2.7 (see also figure 2 in Hirotani, Okamoto 1998).

Let us briefly examine the Lorentz factor distribution. In figure 4, the terminal Lorentz factors computed from (20) for the electic field distribution presented in figure 3, are depicted. At the gap boundaries, the Lorentz factors become less than 10^7. As a result, the particles upscatter the soft photons above 5 TeV only in the gap.

In the next subsection, we consider other two X-ray components in addition to the soft blackbody one and in-

© Astronomical Society of Japan • Provided by the NASA Astrophysics Data System

2000PASJ...52..645H

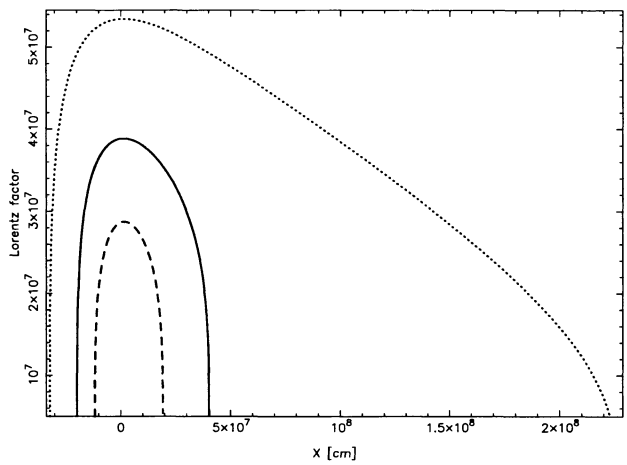

Fig. 4. The distribution of the Lorentz factor. For the solid line, $kT_s = 50$ eV, while for the dashed and the dotted one, 100 and 23.5 eV, respectively. The hard blackbody and the power-law components are not included in this calculation.

vestigate the strength of the inversely Comptonized TeV fluxes.

3.2. *Invisibility of Pulses above 5 TeV*

The relativistic particles produce γ-rays mainly via curvature radiation as described in the preceding sections. However, even though energetically negligible, it is useful to draw attention to the TeV γ-rays produced via inverse-Compton (IC) scatterings. We should notice here that it is the infrared photons with energy ~ 0.1 eV that contribute most effectively as the target photons of IC scatterings. Neither the higher energy photons, like surface blackbody X-rays, nor the lower energy photons, like polar-cap radio emission, contribute as the target photons, because they have either too small cross sections or too small energy transfer when they are scattered.

Assuming that the azimuthal gap width is

$$\pi h \equiv \pi \frac{x_2 - x_1}{\varpi} \text{ rad}, \tag{68}$$

we can estimate the number of particles contained in the gap as

$$N_e \sim \varpi_{LC}{}^3 \left(j_0 \frac{\Omega B}{2\pi ce}\right) \left(\frac{D_\perp}{\varpi_{LC}}\right) \left(2\pi \frac{r_0 \sin\theta_0}{\varpi_{LC}}\right) h^2, \tag{69}$$

where $h \equiv (x_2 - x_1)/(2\varpi_{LC})$ denotes the dimensionless gap half width; $j_0 \Omega B/(2\pi ce)$ indicates the number density of particles. Since the γ-rays have energies less than $\Gamma m_e c^2$, we obtain the luminosity of IC-scattered γ-rays as follows:

$$L_{IC} < N_e \cdot N_{IR} \sigma_T c \cdot \Gamma m_e c^2, \tag{70}$$

where N_{IR} refers to the number density of the infrared photons. Evaluating N_{IR} at the gap center, we obtain

$$N_{IR} \sim \frac{L_{IR}}{4\pi r_0{}^2 c E_{IR}}, \tag{71}$$

where L_{IR} is the infrared luminosity and $E_{IR} \sim 0.1$ eV. We thus obtain

$$L_{IC} < 5.63 \times 10^{-5} B_5 L_{IR} \left(\frac{\varpi_{LC}}{r_0} \sin\theta_0\right) \left(j_0 \frac{D_\perp}{\varpi_{LC}}\right) \times \Gamma h^2 \text{ erg s}^{-1}. \tag{72}$$

The νF_ν flux of IC-scattered γ-rays, $(\nu F_\nu)_{TeV}$ [Jy Hz], can be readily computed as

$$(\nu F_\nu)_{TeV} = 10^{20} \left(\frac{L_{IC}}{\text{erg s}^{-1}}\right) \left(\frac{\omega_{TeV}}{1 \text{ ster}}\right)^{-1} d_1{}^{-2} \text{ Jy Hz}, \tag{73}$$

where ω_{TeV} refers to the solid angle in which the TeV γ-rays are emitted, and $d_1 \equiv d/1$ kpc.

An analogous relation holds for an infrared flux, $(\nu F_\nu)_{0.1\,eV}$, if the infrared luminosity, L_{IR}, is emitted in a solid angle $\omega_{0.1eV}$ ster. We thus obtain the flux ratio

$$f_R \equiv \frac{(\nu F_\nu)_{TeV}}{(\nu F_\nu)_{0.1\,eV}} < 5.63 \times 10^{-5} \left(\frac{\varpi_{LC}}{r_0} \sin\theta_0\right) \times \Gamma \left(j_0 \frac{D_\perp}{\varpi_{LC}}\right) \frac{B}{10^5 \text{ G}} \frac{\omega_{0.1\,eV}}{\omega_{TeV}} h^2. \tag{74}$$

Since we take the ratio of νF_ν flux at two different energies, the uncertainties arising from the distance disappears on the right-hand side. For simplicity, we assume $\omega_{TeV} = \omega_{0.1\,eV}$. As an upper bound, we take $D_\perp/\varpi_{LC} = 1.0$.

Substituting the results of h into equation (74), we obtain the upper bound of f_R. We adopt $j_0 = 0.01$, because the solutions exist for a wide range of parameters such as Ω, μ, kT_s, A_s, kT_h, A_h, α (photon index), and N_{pl}.

We present the results of f_R when the soft blackbody component dominates in figure 5; $A_s = A_*$ and $A_h = N_{pl} = 0$ are assumed. The five curves correspond to the parameter set presented in table 1. It follows that f_R is a decreasing function of kT_s and is not more than 10^2 for a very small kT_s. The filled circles correspond to the minimum allowed temperature below which no solution exists; this corresponds to the dotted curve in figure 5. The open circles, on the other hand, represent kT_s at which the acceleration length of particles equals the gap half width. Above this kT_s, the mono-energetic approximation of particles breaks down.

It is noteworthy that the upper limits of f_R are derived for small j_0 ($= 0.01$). Seemingly, the value of f_R increases for much larger j_0. However, the boundary conditions do not allow a solution to exist above a certain value of j_0 for fixed other parameters. That is, a large j_0 makes the terms $n_+ - n_-$ in equation (11) be large to cancel the

© Astronomical Society of Japan • Provided by the NASA Astrophysics Data System

2000PASJ...52..645H

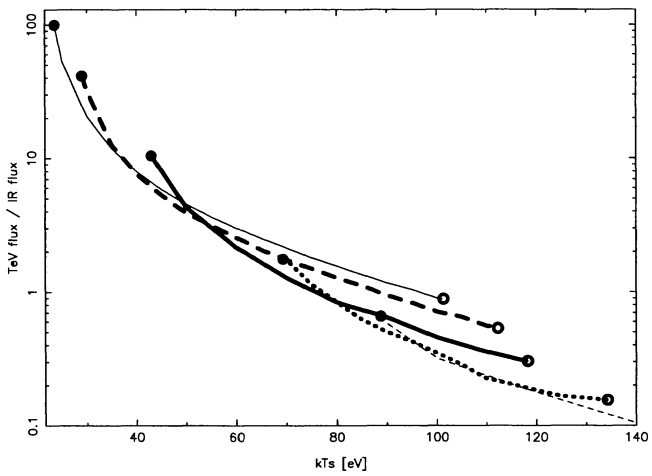

Fig. 5. νF_ν TeV flux vs. soft blackbody temperature. The five curves corresponds to the parameter set presented in table 1. The hard blackbody and the power-law components are not included.

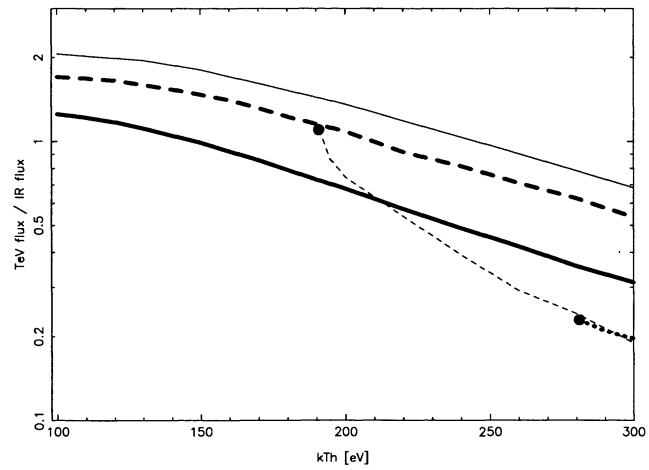

Fig. 6. νF_ν TeV flux vs. hard blackbody temperature. The five curves corresponds to the parameter set presented in table 1. The power-law component is not included.

Table 1. Model parameters for figures 3–7.

	Ω rad s^{-1}	μ G cm^3	α_i degree	$D_\perp$	j_0
thick solid	50	1.0×10^{30}	30	$\varpi_{\rm LC}$	0.01
thick dashed	50	3.0×10^{30}	30	$\varpi_{\rm LC}$	0.01
thick dotted	50	0.3×10^{30}	30	$\varpi_{\rm LC}$	0.01
thin solid	100	1.0×10^{30}	30	$\varpi_{\rm LC}$	0.01
thin dashed	25	1.0×10^{30}	30	$\varpi_{\rm LC}$	0.01

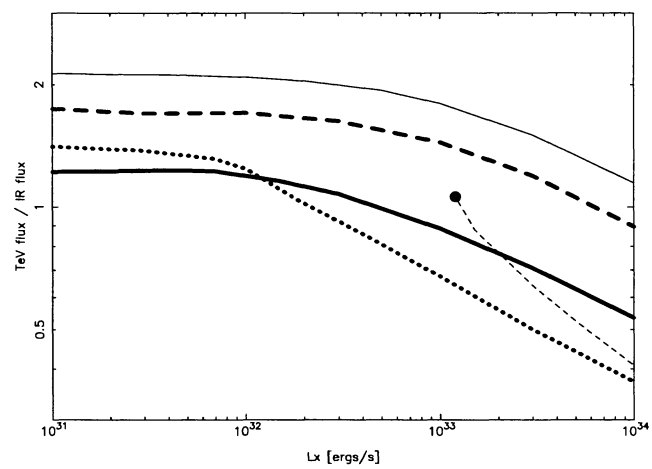

Fig. 7. νF_ν TeV flux vs. power-law luminosity. The five curves corresponds to the parameter set presented in table 1. The hard blackbody component is not included.

term containing $\rho_{\rm GJ}$. As a result, $E_\parallel(\xi)$ has the 'brim' (i.e., $dE_\parallel/d\xi \approx 0$ at the outer boundary) for a large j_0. For example, if we fix the temperature as $kT_{\rm s} = 100$ eV for $\Omega = 100$ rad s^{-1} and $\mu = 10^{30}$ G cm^3, j_0 should be less than 0.594 so that a solution may exist. The value of $f_{\rm R}$ is an increasing function of j_0; however, its value is at most 239 at $j_0 = 0.594$. Furthermore, $f_{\rm R}$ increases with decreasing $kT_{\rm s}$ for a fixed j_0 and other parameters. For example, for $j_0 = 0.03$, $f_{\rm R}$ attains its maximum value at $kT_{\rm s} = 29.9$ eV; below this temperature, no solution exists (see the dotted curve in figure 3). In short, the TeV flux does not greatly exceed a few hundred times of the infrared flux; and such largest values of TeV flux can be realized only when the current density is fine tuned closed to its maximum value for a given set of parameters of Ω, μ, and $kT_{\rm s}$.

When the hard blackbody and/or the power-law components contribute in addition to the soft blackbody emission, the X-ray field becomes stronger to reduce $f_{\rm R}$. To clarify this point, let us briefly consider the cases when the other two components contribute.

First, in figure 6, we present the results when the hard blackbody component dominates. The abscissa indicates $kT_{\rm h}$; $kT_{\rm s} = 70$ eV, $A_{\rm s} = A_*$, $A_{\rm h} = 10^{-2}A_*$, and $N_{\rm pl} = 0$. The five curves correspond to the parameter set presented in table 1. At small $kT_{\rm h}$, $f_{\rm R}$ is bounded by the soft blackbody X-ray field with $kT_{\rm s} = 70$ eV. As a results, $f_{\rm R}$ does not greatly exceed 2.

Secondly, we consider the case when the magnetospheric, power-law component contributes. In figure 7,

© Astronomical Society of Japan • Provided by the NASA Astrophysics Data System

2000PASJ...52..645H

we present the results of $f_{\rm R}$ as a function of the luminosity of the power-law emission, $L_{\rm pl}$, where $L_{\rm pl}$ is related with $N_{\rm pl}$ as

$$N_{\rm pl} = \frac{2-\alpha}{\epsilon_{\rm max}^{2-\alpha} - \epsilon_{\rm min}^{2-\alpha}} \frac{L_{\rm pl}}{4\pi \varpi_{\rm LC}{}^2 m_{\rm e} c^3} \left(\frac{r_0}{\varpi_{\rm LC}}\right)^{-2}. \qquad (75)$$

As the lower and the upper limits of $L_{\rm pl}$, we take 10^{31} and 10^{34} erg s^{-1}, respectively. We fix other parameters as $kT_{\rm s} = 70$ eV, $A_{\rm s} = A_*$, $A_{\rm h} = 0$, and $\alpha = -1.5$, $m_{\rm e}c^2\epsilon_{\rm min} = 100$ eV, and $m_{\rm e}c^2\epsilon_{\rm max} = 50$ keV. It follows that $f_{\rm R}$ is bounded by the soft blackbody emission from the whole neutron star surface and does not exceed greatly 2. On these grounds, we can conclude that $f_{\rm R}$ does not greatly exceed 10^2 for realistic pulsar parameters, regardless of the component dominating the X-ray field.

4. Discussion

In summary, we have developed a one-dimensional model for an outer-gap accelerator immersed in an X-ray radiation field; the X-rays are supplied by the photospheric emission from the neutron star whole surface, thermal emission from the star's polar caps, and/or non-thermal emission from the magnetosphere. As the X-ray field becomes less luminous, the pair-production mean-free path for a γ-ray photon and hence the gap width along the magnetic field line enlarges. It follows from the Poisson equation that the enlarged gap width results in the increase of the acceleration field (figure 3). As a result, the gap becomes most active when the surface blackbody temperature is small and when neither the polar cap nor the magnetospheric emissions contribute. Even in this case, the flux above 5 TeV does not greatly exceed 10^2 times the infrared flux. We can therefore conclude that the difficulty of excessive TeV emission, which appears in the CHR picture, does not arise in the present outer-gap model for a moderate infrared flux ($< 10^9$ Jy Hz), if we confine the argument to above 5 TeV.

The IR photons can be upscattered above 5 TeV only within the small-volume gap (figure 4). However, the particle Lorentz factor is kept above several times 10^6 even outside of the gap; therefore, the gap volume may be underestimated if we extend our discussion into somewhat lower energies around TeV. On thses grounds, the visibility of γ-ray pulses *below* 5 TeV calls for further consideration. More precisely, the energy (5 TeV, say) above which no γ-rays are emitted outside the gap, should be examined based on the equations of particle motion at the gap boundaries of individual pulsars.

Let us consider how the structure of $E_\parallel(x)$ depends on j_0. In figure 8, we present the distribution of $E_\parallel$ for three values of j_0. In this figure, we fix the parameters as $\alpha_{\rm inc} = 30°$, $\Omega = 100$ rad s^{-1}, $\mu = 10^{30}$ G cm^3,

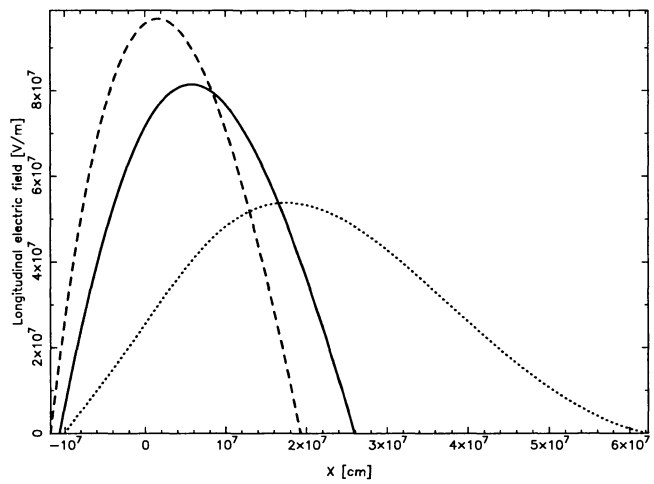

Fig. 8. The distribution of the acceleration field along the field line. For the dashed line, $j_0 = 0.01$, while for the solid and the dotted one, 0.03 and 0.0592 eV, respectively. The hard blackbody and the power-law components are not included in this calculation.

$kT_{\rm s} = 100$ eV; the hard blackbody and the power-law components are not included. The dashed, solid, and the dotted curves correspond to $j_0 = 0.01$, 0.03, and 0.0592. Above $j_0 = 0.0592$, no solutions exist. The dashed curve coincides with the dashed one in figure 3.

It is worth noting that a 'brim' is formed at the inner boundary in figure 3 of Paper III, while it is formed at the outer boundary in figures 3 and 8 of the present paper. In Paper III, the two-dimensional effect prevents the gap to have a brim at the outer boundary. In the present paper, we get rid of such effects by setting $D_\perp = \varpi_{\rm LC}$. Therefore, the brim is formed at the outer boundary, where $\rho_{\rm GJ}$ becomes very small.

We briefly discuss the validity of the rectilinear approximation. In figure 3, the full gap width becomes 10.3% and 14.7% of the light cylinder radius for $kT_{\rm s} = 100$ and 70 eV, respectively, while it becomes 85.5% for 23.5 eV. Therefore, the assumption of the rectilinear coordinates does not seem to be very good for the neutron star that has a very small surface temperature. Nevertheless, for pulsars with a surface temperature less than 100 eV, thermal emissions from heated polar caps may contribute in addition to the whole surface blackbody emission to reduce the gap width. For example, middle-aged pulsars B1055 − 52 and B0656 + 14 (Greiveldinger et al. 1996), or millisecond pulsar J0437 − 4715 (Zavlin, Pavlov 1998) exhibit a thermal hard X-ray component in addition to the soft blackbody one. On these grounds, we consider that the rectilinear approximation holds well for the outer gaps of realistic pulsars.

Let us finally discuss the reason why our analysis re-

© Astronomical Society of Japan • Provided by the NASA Astrophysics Data System

2000PASJ...52..645H

sults in a significantly smaller TeV flux compared with that given by Zhang and Cheng (1998). In the present analysis, the gap occupies only a small fractional space in the magnetosphere. On the other hand, the thick outer–gap model proposed by Zhang and Cheng (1998) occupies a large fractional space. The difference of the gap volume mainly comes from the difference in the presumed soft photon field: Zhang and Cheng (1998) considered the case when the soft photon field results from the bombardment of the return current. In their method, bombardment is self-consistently important, because the return particle flux is large owing to a large fractional volume of the magnetosphere occupied by the outer gap. On the other hand, in the present paper, we consider that the X-ray fields are externally given from observations. The resultant small-volume gap provides so small particle fluxes that the bombardment is relatively unimportant. In the case of middle-aged (or post-Vela) pulsars, however, the outer gap is no longer small-volume. For example, the full gap width along the field lines attains 40% of $\varpi_{\rm LC}$ for B1055 − 52 (Hirotani 2000a). Nevertheless, for such pulsars, the magnetic field, and hence $E_{\parallel}$ in the gap, is so weak that the particles cannot produce copious TeV γ-rays above the detection limit of ground-based telescopes.

This research owes much to the helpful comments of Dr. S. Shibata. The author wishes to express his gratitude to Drs. Y. Saito and A. Harding for valuable advice. He also thanks the Astronomical Data Analysis Center of National Astronomical Observatory, for the use of workstations.

References

Aschenbach B., Brinkmann W. 1975, A&A 41, 147
Berestetskii V.B., Lifshitz E.M., Pitaevskii L.P. 1989, Quantum Electrodynamics 3rd ed
Cheng K.S. 1994, in Towards a Major Atmospheric Cerenkov Detector III, (Universal Academy Press, Tokyo) p25
Cheng K.S., Ho C., Ruderman M. 1986a, ApJ 300, 500 (CHR86a)
Cheng K.S., Ho C., Ruderman M. 1986b, ApJ 300, 522 (CHR86b)
Cheng K.S., Zhang L. 1998, ApJ 498, 327
Chiang J., Romani R.W. 1992, ApJ 400, 629
Chiang J., Romani R.W. 1994, ApJ 436, 754
Daishido T. 1975, PASJ 27, 181
Daugherty J., Harding A.K. 1982, ApJ 252, 337
Daugherty J., Harding A.K. 1996, ApJ 458, 278
Dermer C.D., Sturner, S.I. 1994, ApJ 420, L75
Edwards P.G., Thornton G.J., Patterson J.R., Roberts M.D., Rowell G.P. 1994, A&A 291, 468
El-Gowhari A., Arponen J. 1972, Nuovo Cimento 11B, 201
Fierro J.M., Michelson P.F., Nolan P.L., Thompson D.J. 1998, ApJ 494, 734
Gil J.A., Krawczyk A. 1996, MNRAS 285, 566
Greenstein G., Hartke G.J. 1983, ApJ 271, 283
Greiveldinger C., Camerini U., Fry W., Markwardt C.B., Ögelman H., Safi-Harb S., Finley, J.P., Tsuruta S. 1996, ApJ 465, L35
Hardee P.E., Rose W.K. 1974, ApJ 194, L35
Harding A.K., Tademaru E., Esposito L.W., 1978, ApJ 225, 226
Hirotani K. 2000a, MNRAS in press (Paper IV)
Hirotani K. 2000b, ApJ submitted (Paper V)
Hirotani K., Okamoto I. 1998, ApJ 497, 563
Hirotani K., Shibata S. 1999a, MNRAS 308, 54 (Paper I)
Hirotani K., Shibata S. 1999b, MNRAS 308, 67 (Paper II)
Hirotani K., Shibata S. 1999c, PASJ 51, 683 (Paper III)
Kanbach G., Arzoumanian Z., Bertsch D.L., Brazier K.T.S., Chiang J., Fichtel C.E., Fierro J.M., Hartman R.C. et al. 1994, A&A 289, 855
Kaspi V.M., Lackey J.R., Manchester R.N., Bailes M., Pace R. 2000, ApJ 528, 445
Kifune T. 1996, Space Sci. Rev. 75, 31
Krause-Polstorff J., Michel F.C. 1985a, MNRAS 213, 43
Krause-Polstorff J., Michel F.C. 1985b, A&A 144, 72
Kundt W., Schaaf R. 1993, Ap&SS 200, 251
Mayer-Hasselwander H.A., Bertsch D.L., Brazier T.S., Chiang J., Fichtel C.E., Fierro J.M., Hartman R.C., Hunter S.D. 1994, ApJ 421, 276
Michel F.C. 1974, ApJ 192, 713
Miyazaki J., Takahara F. 1997, MNRAS 290, 49
Nel H.I., Arzoumanian Z., Bailes M., Brazier K.T.S., D'Amico N., Esposito J.A., Fichtel C.E., Fierro J.M. 1996, ApJ 465, 898
Nel H.I., de Jager O.C., Raubenheimer B.C., Brink C., Meintjes P.J., Nortt A.R. 1993, ApJ 418, 836
Nolan P.L., Arzoumanian Z., Bertsch D.L., Chiang J., Fichtel C.E., Fierro J.M., Hartman R.C., Hunter S.D. et al. 1993, ApJ 409, 697
Nolan P.L., Fierro J.M., Lin Y.C., Michelson P.F., Bertsch D.L., Dingus B.L., Esposito J.A., Fichtel C.E. et al. 1996, A&AS 120, 61
Ochelkov Yu.P., Usov V.V. 1980a, Ap&SS 69, 439
Ochelkov Yu.P., Usov V.V. 1980b, SvAL 6, 414
Pavlov G.G., Shibanov Yu.A., Ventura J., Zavlin V.E. 1994, A&A, 289, 837
Ramanamurthy P.V., Bertsch D.L., Dingus L., Esposito J.A., Fierro J.M., Fichtel C.E., Hunter S.D., Kanbach G. et al. 1995, ApJ 447, L109
Ramanamurthy P.V., Fichtel C.E., Kniffen D.A., Sreekumar P., Thompson D.J. 1996, ApJ 458, 755
Romani R.W. 1987, ApJ 313, 718
Romani R.W. 1996, ApJ 470, 469
Romani R.W., Yadigaroglu I. 1995, ApJ 438, 314
Rybicki G.B., Lightman A.P. 1979, Radiative processes in astrophysics (John Wiley & Sons, New York)
Saito Y. 1998, PhD Thesis, The University of Tokyo
Scharlemann E.T., Arons J., Fawley W.M. 1978, ApJ 222, 297
Shibanov Yu.A., Zavlin V.E., Pavlov G.G., Ventura J. 1995, A&A 266, 313
Shibata S. 1997, MNRAS 287, 262
Shibata S., Miyazaki J., Takahara F. 1998, MNRAS 295, L53

© Astronomical Society of Japan • Provided by the NASA Astrophysics Data System

2000PASJ...52..645H

Sturner S.J., Dermer C.D., Michel F.C. 1995, ApJ 445, 736
Thompson D.J., Bailes M., Bertsch D.L., Cordes J., D'Amico N., Esposito J.A., Finley J., Hartman R.C. et al. 1999, ApJ 516, 297
Thompson D.J., Bailes M., Bertsch D.L., Esposito J.A., Fichtel C.E., Harding A.K., Hartman R.C., Hunter S.D. 1996, ApJ 465, 385
Ulmer M.P. 1994, ApJS 90, 789
Usov V.V. 1994, ApJ 427, 394
Yoshikoshi T., Kifune T., Dazeley S.A., Edwards P.G., Hara T., Hayami Y., Kakimoto F., Konishi T. 1997, ApJ 487, L65
Zavlin V.E., Pavlov G.G. 1998, A&A 329, 583
Zavlin V.E., Pavlov G.G., Shibanov Yu.A., Ventura J. 1995a, A&A 297, 441
Zavlin V.E., Shibanov Yu.A., Pavlov G.G. 1995b, Astron. Lett. 21, 149
Zhang L., Cheng K.S. 1998, MNRAS 294, 177

© Astronomical Society of Japan • Provided by the NASA Astrophysics Data System